CrossMark

J. Fluid Mech. (2018), *vol.* 848, *pp.* 821–835. © Cambridge University Press 2018
doi:10.1017/jfm.2018.383

Early azimuthal instability during drop impact

E. Q. Li[1,2], M.-J. Thoraval[1,3], J. O. Marston[1,4] and S. T. Thoroddsen[1,†]

[1]Division of Physical Sciences and Engineering, King Abdullah University of Science and Technology (KAUST), Thuwal, 23955-6900, Saudi Arabia

[2]Department of Modern Mechanics, University of Science and Technology of China, Hefei 230027, PR China

[3]State Key Laboratory for Strength and Vibration of Mechanical Structures, Shaanxi Key Laboratory of Environment and Control for Flight Vehicle, International Center for Applied Mechanics, School of Aerospace, Xi'an Jiaotong University, Xi'an 710049, PR China

[4]Department of Chemical Engineering, Texas Tech University, Lubbock, TX 79409-3121, USA

(Received 29 January 2018; revised 29 April 2018; accepted 3 May 2018;
first published online 13 June 2018)

When a drop impacts on a liquid surface its bottom is deformed by lubrication pressure and it entraps a thin disc of air, thereby making contact along a ring at a finite distance from the centreline. The outer edge of this contact moves radially at high speed, governed by the impact velocity and bottom radius of the drop. Then at a certain radial location an ejecta sheet emerges from the neck connecting the two liquid masses. Herein, we show the formation of an azimuthal instability at the base of this ejecta, in the sharp corners at the two sides of the ejecta. They promote regular radial vorticity, thereby breaking the axisymmetry of the motions on the finest scales. The azimuthal wavenumber grows with the impact Weber number, based on the bottom curvature of the drop, reaching over 400 streamwise streaks around the periphery. This instability occurs first at Reynolds numbers (Re) of $\sim$7000, but for larger Re is overtaken by the subsequent axisymmetric vortex shedding and their interactions can form intricate tangles, loops or chains.

Key words: capillary flows, drops and bubbles, interfacial flows (free surface)

1. Introduction

The dynamics surrounding the earliest contact of an impacting drop determines the vigour of droplet splashing and the amount of small bubbles entrained into the pool. Following in the footsteps of Worthington (1908), drop impact studies have through the decades relied on advances in imaging technology (Etoh *et al.* 2003; Thoroddsen *et al.* 2008). Most early studies have focused on the breakup of the crown (Deegan *et al.* 2008), crater formation and collapse (Prosperetti *et al.* 1989) or air entrapment under its centre (Thoroddsen *et al.* 2003; Hendrix *et al.* 2016). The latest improvements in imaging, which include video cameras with sub-micro-second time resolution (Crooks *et al.* 2013) used herein, as well as high-speed X-ray imaging (Zhang *et al.* 2012), are now revealing the finest details of this dynamics.

† Email address for correspondence: Sigurdur.Thoroddsen@KAUST.edu.sa

https://doi.org/10.1017/jfm.2018.383 Published online by Cambridge University Press

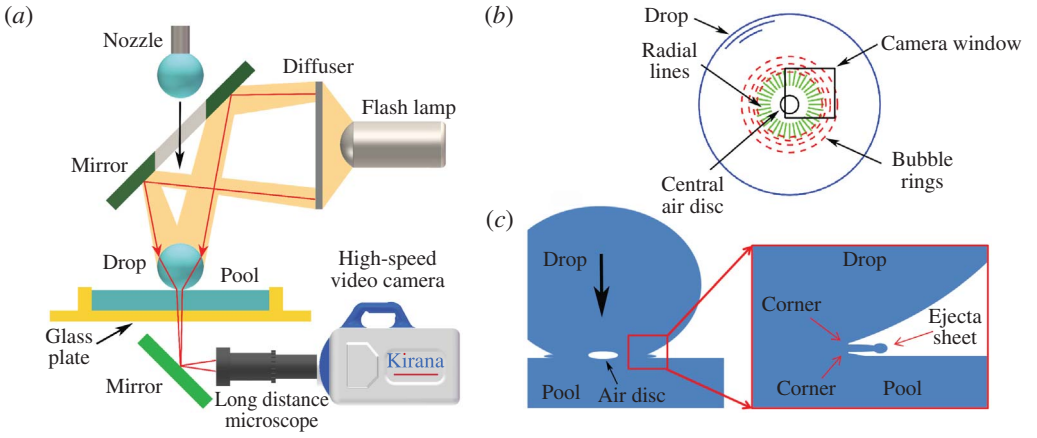


FIGURE 1. (Colour online) (*a*) Sketch of the experimental configuration, showing the drop release from a steel nozzle fed by a syringe pump. The drop subsequently falls through a hole in a mirror onto the liquid film contained above a glass surface, with the camera viewing the impact vertically through the bottom. (*b*) The typical area of the camera view relative to the size of the drop. (*c*) Sketch of the neck with ejecta and two sharp corners at its base.

For medium drop impact velocities on a liquid pool, a prominent feature is the ejecta sheet which is the first stage leading to splashing. It was first revealed in the inviscid numerical simulations of Weiss & Yarin (1999) and observed in the experiments of Thoroddsen (2002). The breakup of this ejecta sheet produces the splashing of the finest spray, which is important, for example, for aerosol formation. Thoraval *et al.* (2012) discovered that the transition to random splashing is associated with Kármán-type vortex shedding from the base of the ejecta, which can destabilize and break it up. This vortex shedding was imaged by Castrejon-Pita *et al.* (2012) and Thoraval *et al.* (2013).

Herein, we use an ultra-high-speed video camera to achieve extreme space and time resolution to identify an earlier capillary-driven instability, which forms in the two sharp corners surrounding the base of the ejecta sheet, at impact Reynolds numbers lower than that needed for axisymmetric shedding.

2. Experimental set-up

2.1. *Imaging set-up*

The experimental configuration is shown in figure 1(*a*) and consists of a drop released from a nozzle and subsequently falling through a hole in a mirror onto the liquid film contained above a glass surface. The mirror allows flash illumination nearly down the vertical axis of the drop. The drop also focuses the light to intensify the light near its centre. The sharp slope of the drop limits imaging near its edge. The camera views the impact through the bottom, using a long-distance microscope (Leica Z16 APO) with adjustable magnification and aperture. Magnifications as large as 29.2 were used, giving a corresponding pixel resolution of up to 1.04 μm px^{-1}. The rapid initial motions were observed with a high-speed video camera (Kirana-05M, Specialized Imaging, Tring UK) at frame rates up to 5 million fps (Crooks *et al.* 2013). This camera takes 180 frames each with 924 $\times$ 768 pixels. Most video clips were acquired at between 0.5 and 2 Mfps, with exposure durations down to 100 ns

https://doi.org/10.1017/jfm.2018.383 Published online by Cambridge University Press

per frame, to minimize motion smearing. This required intense lighting with a 300 W high-power flash of short duration (∼400 μs) (Specialized Imaging, SI-AD 500), which encompasses the entire span of the video clip.

2.2. *Liquids and drop shapes*

We used common mineral water (Highland Springs) for the drops, while dissolving sodium-chloride (NaCl) to form a salt solution in the film liquid. This generates a strong mismatch in the refractive index, to aid the imaging of disturbances and vortices at the liquid–liquid interface. The pool depth was kept at $\simeq 1$ mm by depositing a fixed amount of the salt solution into a circular glass dish containing the bottom pool. This is sufficiently deep to minimize depth effects during the early contact (Thoraval *et al.* 2013). The surface tensions were measured using a ring tensiometer (K100 MK2/SF/C, Kruss GmbH, Hamburg), giving $\sigma = 71.8$ mN m^{-1} for the drop and slightly higher value for the salt solution, 73.4 (quarter saturation), 75.0 (half-saturation) and 76.9 (fully saturated) mN m^{-1}. Unless otherwise stated, we use the saturated salt solution with a density of 1.19 g cm^{-3}.

The drop is pinched off from a tapered stainless steel nozzle with a sharp inner edge of ∼3 mm in diameter. The resulting drop is axisymmetric with an equivalent spherical diameter of $D = 4.23$ mm. The release heights H, measured from the nozzle to the pool surface, were varied from $H = 14.5$–59.6 cm, giving impact velocities of between $U = 1.6$–3.3 m s^{-1}. We characterize the impact conditions by the Reynolds and Weber numbers,

$$Re = \frac{\rho D U}{\mu}, \quad We = \frac{\rho D U^2}{\sigma}, \tag{2.1a,b}$$

where μ and σ are the dynamic viscosity and surface tension of the drop liquid. We use the average density of the drop and pool, ρ.

The impact velocities and droplet shapes were measured in a separate set of experiments, as described in the supplementary material available at https://doi.org/10.1017/jfm.2018.383. As the drop is larger than the capillary length for water, significant shape oscillations occur after the pinch off during the free fall. We follow the approach described in Thoraval *et al.* (2013) to characterize the drop shape by an aspect ratio $\alpha = D_V/D_H$, where D_H and D_V are the horizontal and vertical diameters of the drop at impact. By assuming an elliptic drop shape we can estimate the bottom radius of curvature, as $R_b \simeq D/(2\alpha^{4/3})$. To include this drop shape we therefore define a modified $Re_\alpha = Re/\alpha^{4/3}$ and $We_\alpha = We/\alpha^{4/3}$. Table 1 lists the various impact parameters used herein.

3. Results

3.1. *Speed of neck radius*

Having sufficient time resolution we can accurately measure the initial motions of the outer radius of the neck contact R_n, as is shown in figure 3(*a*) for typical cases. We plot this radius normalized by the drop bottom radius R_b, which includes the above aspect ratio estimation, $r(\tau) = R_n(\tau)/R_b$. Similarly, we normalize the time with an adjustable offset, as $\tau = (t - t_o)U/R_b$. The simplest possible model of the initial neck motions is based on purely geometric considerations, i.e. that of a sphere cutting a plane, where the intersection moves outwards as $\sqrt{2\tau}$ (Rioboo *et al.* 2002; Josserand & Zaleski 2003), see also discussion in Philippi *et al.* (2016). However, this model does not satisfy continuity which requires modifying the prefactor. On the other hand, including Wagner inviscid theory for liquid impact on a solid (Wagner 1932; Scolan

https://doi.org/10.1017/jfm.2018.383 Published online by Cambridge University Press

Impact height H (cm)	Impact velocity U (m s^{-1})	Aspect ratio α D_V/D_H	Re	Re_α	We	We_α	C	t_o (μs)	$\langle N \rangle$	Air disc R_{air}/R_b
14.5	1.64	1.047	6 870	6 510	172	163	1.16	4.2	—	0.150
17.5	1.80	1.164	7 560	6 220	208	171	1.08	4.9	118	0.134
20.3	1.94	0.791	8 140	11 200	242	333	1.05	4.9	153	0.097
23.0	2.06	1.198	8 670	6 860	274	217	0.98	4.0	134	0.112
27.3	2.25	1.063	9 440	8 760	325	302	1.03	3.5	215	0.122
30.8	2.38	0.828	10 020	13 000	366	473	1.20	3.1	241	0.113
36.0	2.57	1.058	10 800	10 100	426	398	1.04	2.8	229	0.110
40.2	2.71	1.090	11 400	10 200	474	425	1.12	2.4	225	0.116
42.7	2.79	1.080	11 700	10 700	502	456	1.03	1.9	183	0.104
45.3	2.87	0.787	12 070	16 700	531	737	1.15	2.8	420	0.096
47.8	2.95	1.139	12 380	10,500	559	474	1.13	2.6	254	0.118
50.3	3.02	1.063	12 680	11 800	587	545	1.02	2.3	234	0.102
52.8	3.09	0.790	12 980	17 900	614	848	1.27	2.5	400	0.109
54.3	3.13	0.943	13 150	14 300	630	687	1.01	1.7	287	0.087
55.3	3.16	1.112	13 260	11 600	642	561	0.86	1.5	286	0.105
57.8	3.22	1.131	13 540	11 600	669	572	1.07	1.9	319	0.108
59.6	3.27	0.874	13 740	16 600	688	830	1.07	1.9	360	0.091

TABLE 1. Parameters and experimental results for the various impact release heights. C and t_o are fitting coefficients used in (3.1). $\langle N \rangle$ is the average number of radial lines rounded off to the nearest integer. The initial air-disc diameter d_{air} is normalized by twice the bottom radius of drop R_b.

& Korobkin 2001; Korobkin & Scolan 2006; Riboux & Gordillo 2014; Philippi *et al.* 2016) the radial motions take the functional form

$$r(\tau) = C\sqrt{3\tau}, \tag{3.1}$$

where theoretically $C = 1$. Here we use C and t_o as fitting coefficients, which are listed in table 1 for all of the impact heights. The value of C is close to unity, with an average of 1.07, which supports the validity of (3.1) above. The significant spread in the values of C are likely caused by the drops being an elliptic paraboloid resulting in $C(\alpha)$, as can be inferred by theoretical considerations (Scolan & Korobkin 2001; Oliver 2002; Korobkin 2007). However, to characterize this $C(\alpha)$ one would need high-resolution concurrent measurements of the drop shape from a second side-view video camera.

The full Navier–Stokes simulations of Thoraval *et al.* (2012) of the initial neck radius versus time are in perfect agreement with (3.1), showing (after modifying the notation) $r(\tau) = 1.004\sqrt{3\tau}$.

The initial velocity of the neck is therefore $\mathrm{d}R_n/\mathrm{d}t = C\sqrt{3R_bU/4(t-t_o)}$. For the largest Re_α this speed is 54 m s^{-1}, or ∼17 times the impact velocity, which is significantly faster than the ejecta sheet ∼10 (Thoroddsen 2002), which emerges later on.

3.2. *Onset of front instability and radial lines*

Figure 2 shows the regular teeth-like pattern in the neck region connecting the drop to the pool liquid. Here the distance between the adjacent teeth is ∼17 μm and they

https://doi.org/10.1017/jfm.2018.383 Published online by Cambridge University Press

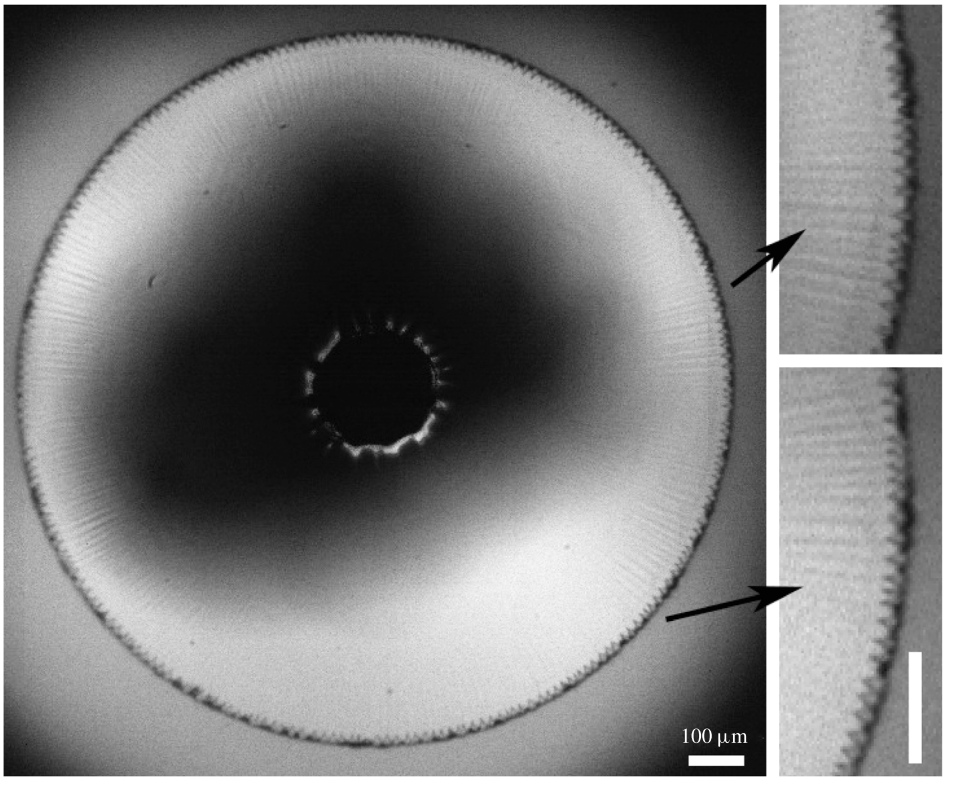


FIGURE 2. Regular teeth in the neck connecting the drop to the pool, with radial lines extending from these teeth into the interface between the drop and pool liquid. For $U = 2.71$ m s^{-1}, $\alpha = 1.09$, giving $Re_\alpha = 10\,200$ and $We_\alpha = 425$. Outside this circle the drop has not yet contacted the pool. The central irregular circle is the outer edge of the entrapped air disc. Keep in mind that the drop diameter, $D = 4.23$ mm, is three times larger than the width of this image. The darker section in the middle of the image arises from the hole in the mirror, through which the drop falls. Both scale bars are 100 μm long.

are seen around the entire periphery. The image shows radial lines extending from these teeth into the liquid in the neck. These lines are visible through the index of refraction difference between the drop and pool liquids, manifesting localized vertical motions which we associated with streamwise vorticity. Each radial line may consist of two counter-rotating streamwise vortices. We infer the presence of these vortices by their subsequent sideways interactions, as is evident in figure 4(*a*).

These frontal undulations appear when $Re \sim 7000$ and $We \sim 200$. For lower impact heights the front remains straight, as shown in supplementary figure S3. This is not a sharp boundary and weak undulations can occur at larger radii, for lower Re, as was shown in Thoraval *et al.* (2013), but no well-defined teeth appear.

Figure 3(*b*) shows the initial radius of the central air disc R_{air}. This disc has been extensively studied, especially for drop impacts on a solid surface, see Josserand & Thoroddsen (2016). This entrapment is characterized by balancing the viscous lubrication pressure in the air with the drop inertia, giving rise to the Stokes number $St = \mu_g/(\rho_\ell U R_b)$ (Korobkin *et al.* 2008; Marston *et al.* 2011; Bouwhuis *et al.* 2012). For atmospheric ambient pressure, Li & Thoroddsen (2015) verified the theoretical

https://doi.org/10.1017/jfm.2018.383 Published online by Cambridge University Press

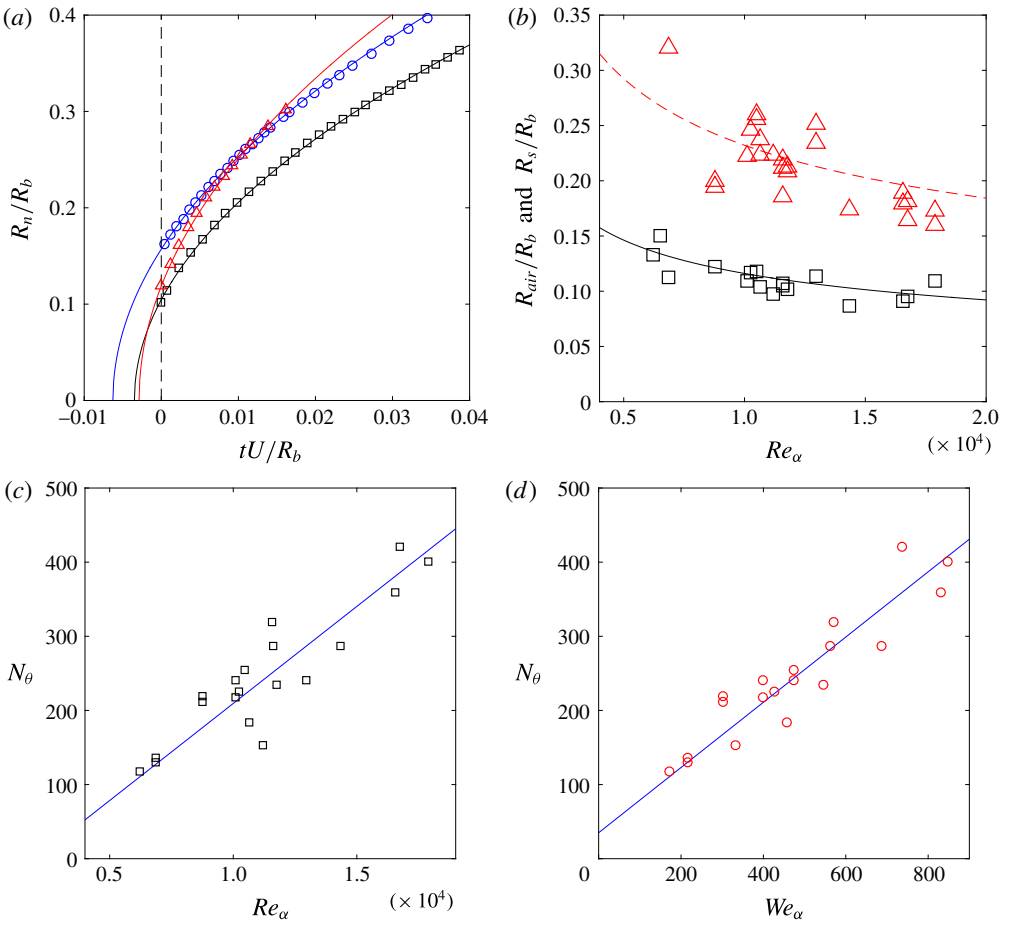


FIGURE 3. (Colour online) (*a*) The radial motion of the outer edge of the neck contact, for $U = 1.64$ m s^{-1}, $Re_\alpha = 6510$ (blue circle); $U = 3.02$ m s^{-1}, $Re_\alpha = 11\,800$ (black square); $U = 3.09$ m s^{-1}, $Re_\alpha = 17\,900$ (red triangle). Solid lines are fits using (3.1), with coefficients given in table 1. (*b*) Size of the central air disc (black squares) and radius R_s at onset of radial lines (red triangles). The black curve corresponds to (3.2), with $C_2 = 1.35$, while the top dashed curve shows double this radius, with $C_2 = 2.70$. (*c*,*d*) Total number of radial lines around the periphery, versus Re_α and We_α. Keep in mind that both R_b and U change for these data, as listed in table 1.

axisymmetric prediction of Hicks & Purvis (2010) and Hicks *et al.* (2012) that $R_{air}/R_b = (3.8 \times 4^{1/3})\, St^{1/3}$, for a drop impacting a solid surface, without adjustable constants. For impacts onto a liquid surface, Tran *et al.* (2013) and Hendrix *et al.* (2016) have shown that one should use half the impact velocity $U/2$, when evaluating St to account for the compliance of the free-surface substrate. In the figure we therefore include the fit,

$$\frac{R_{air}}{R_b} = C_2\,(3.8 \times 4^{1/3})\, St^{1/3} = C_2(3.8 \times 4^{1/3}) \left(\frac{2\mu_g}{\mu_\ell}\right)^{1/3} \left(\frac{Re_\alpha}{2}\right)^{-1/3}, \qquad (3.2)$$

where $C_2 = 1.0$.

https://doi.org/10.1017/jfm.2018.383 Published online by Cambridge University Press

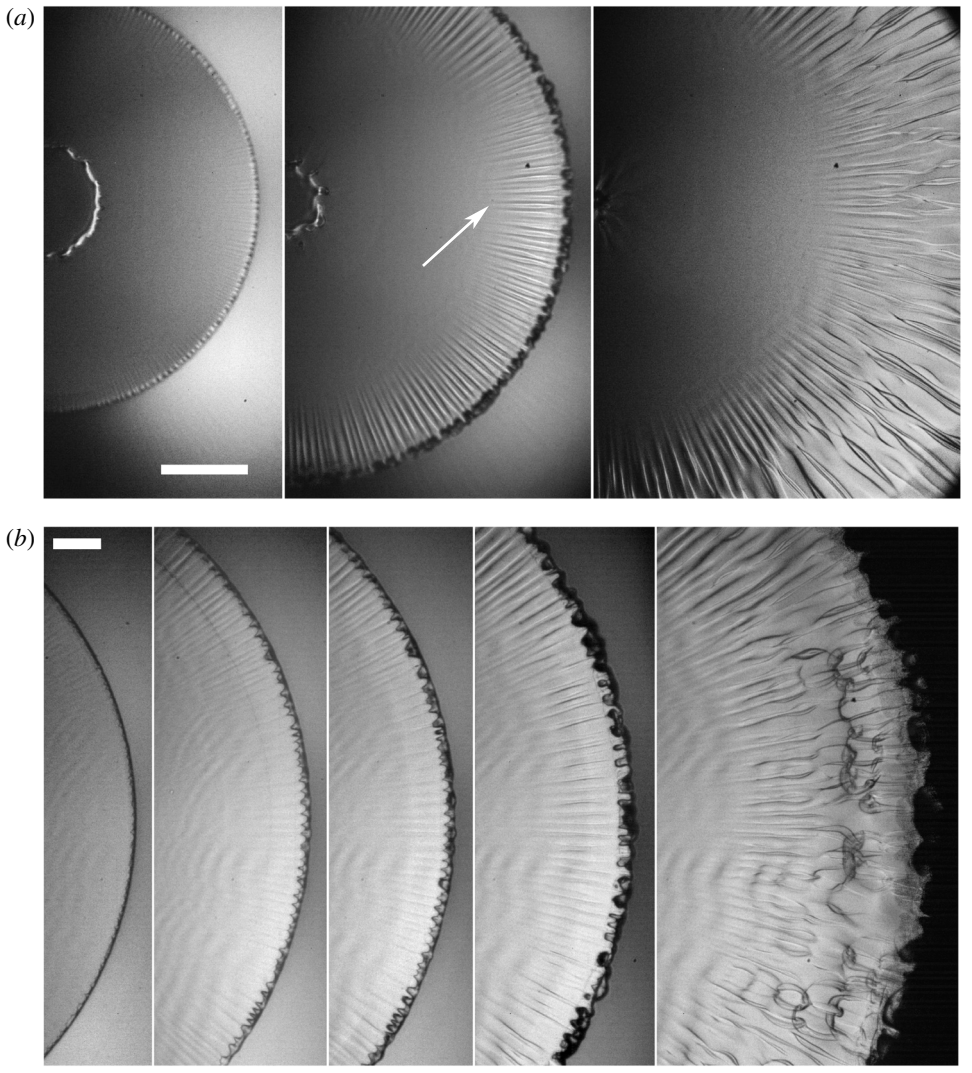


FIGURE 4. The evolution of the edge instability and radial lines, for (*a*) $U = 3.02$ m s^{-1}, $D = 4.23$ mm and $\alpha = 1.063$, giving $Re_\alpha = 11\,800$ and $We_\alpha = 545$. Frames shown 10, 20 and 70 μs after first contact. The scale bar is 200 μm long. (*b*) Evolution of the front, for $U = 2.38$ m s^{-1}, $\alpha = 0.828$, giving $Re_\alpha = 13\,000$ and $We_\alpha = 473$. Times shown at $t = 16$, 22, 24, 31, 56 μs from first contact. Scale bar is 100 μm long. See supplementary movies 1 and 2.

Figure 3(*b*) also shows the radius R_s, where the radial lines become visible, see arrow in figure 4(*a*). This distance is approximately twice the size of R_{air}. For this second curve, we simply set $C_2 = 2.0$. The large spread in these data, arises from the sensitivity of the visualization technique to illumination angle.

Figure 4(*a*) shows the time evolution of these azimuthal disturbances and the radial lines, for $Re_\alpha = 11\,800$. The triangular shapes are overtaken by air sheets with more rounded edges, which look similar to those seen in Thoraval *et al.* (2013) (their figure 5). The radial lines, inside the liquid, remain straight in the beginning, but after 70 μs they are clearly winding up around the radial direction, as can be expected for

https://doi.org/10.1017/jfm.2018.383 Published online by Cambridge University Press

interacting streamwise vortices. Here the radial distance from the axis of symmetry to the start of the first visible radial lines, appear when the radius of the contact is 402 μm, or 19 % of the drop radius, see arrow in figure 4(*a*). This coincides with the emergence of the ejecta sheet (Thoroddsen 2002). These frames also show the rapid capillary-driven contraction of the micron thick central air disc, as studied by Thoroddsen *et al.* (2003).

For slightly larger $Re_\alpha = 13\,000$, in figure 4(*b*), we see the beginning of axisymmetric vortex shedding (Thoraval *et al.* 2013), with weak intensity undulations in the second frame, followed by short segments of shed vortices in the last frame. For significantly larger $Re_\alpha = 16\,700$, in figure 5(*a*), we see clear coexistence of azimuthal and radial lines. The second panel shows entrainment of a regular air cylinder (arrow). Figure 5(*b*) shows an identical impact at a smaller optical magnification, where most of the periphery is visible, revealing multiple rows of continuous azimuthal vortices. The axisymmetry is far from perfect, with numerous defects and reconnections. However, the number and spacing of the vortices is essentially identical around the entire periphery.

The number of radial lines increases with the impact velocity. Figure 3(*c*,*d*) shows how this total number of lines around the periphery increases with Re_α and We_α respectively.

Figure 6 shows frame sequences of the formation and breakup of the azimuthal pattern. In (*a*) we show the growing amplitude of the triangular teeth, which saturates in ∼5 μs. In (*b*) we show later evolution of larger air sheets, which overlap and must therefore be pulled in in the sharp corners on both sides of the base of the ejecta sheet (see sketch in figure 1*c*).

4. Discussion and conclusions

4.1. *Possible effect of density difference between drop and pool*

Herein we use different liquids for the drop and pool to enable the visualization. The resulting density difference between the two could affect the dynamics. While this may modify the details, we are convinced this is not the driving force behind the observed phenomena on the following grounds: it is encouraging that the axisymmetric vortex shedding does not change significantly when we reverse the density difference by impacting a water drop on a lighter ethanol pool ($\rho_p/\rho_d \simeq 0.79$ in Thoraval *et al.* (2013)) or onto a denser salt-saturated pool ($\rho_p/\rho_d \simeq 1.19$). Furthermore, Thoraval *et al.* (2013) showed that bubble rings are entrained during identical-density water-on-water impacts. Their numerical simulations used the same liquid properties in drop and pool and showed quantitatively consistent results with the experiments, as far as the axisymmetric shedding.

This is also true for the early azimuthal instability studied herein. To verify this we performed a separate set of experiments with a half and a quarter of the salt concentration in the pool, seeing similar results. Finally, some experiments were done with pure water in both drop and pool. Here we can only observe the presence of the azimuthal instability at the interface, as the refractive index difference is now gone. Figure 7 compares the front shapes for the two cases. Panel (*b*) shows the continued presence of the teeth in the sharp corners, which look the same as with the saturated salt solution in part (*a*). However, there remains an element of doubt about the presence of the radial lines. Experiments with a truly passive scalar, such as a fluorescent dye, could clarify this, but are not possible with the current optical set-up.

https://doi.org/10.1017/jfm.2018.383 Published online by Cambridge University Press

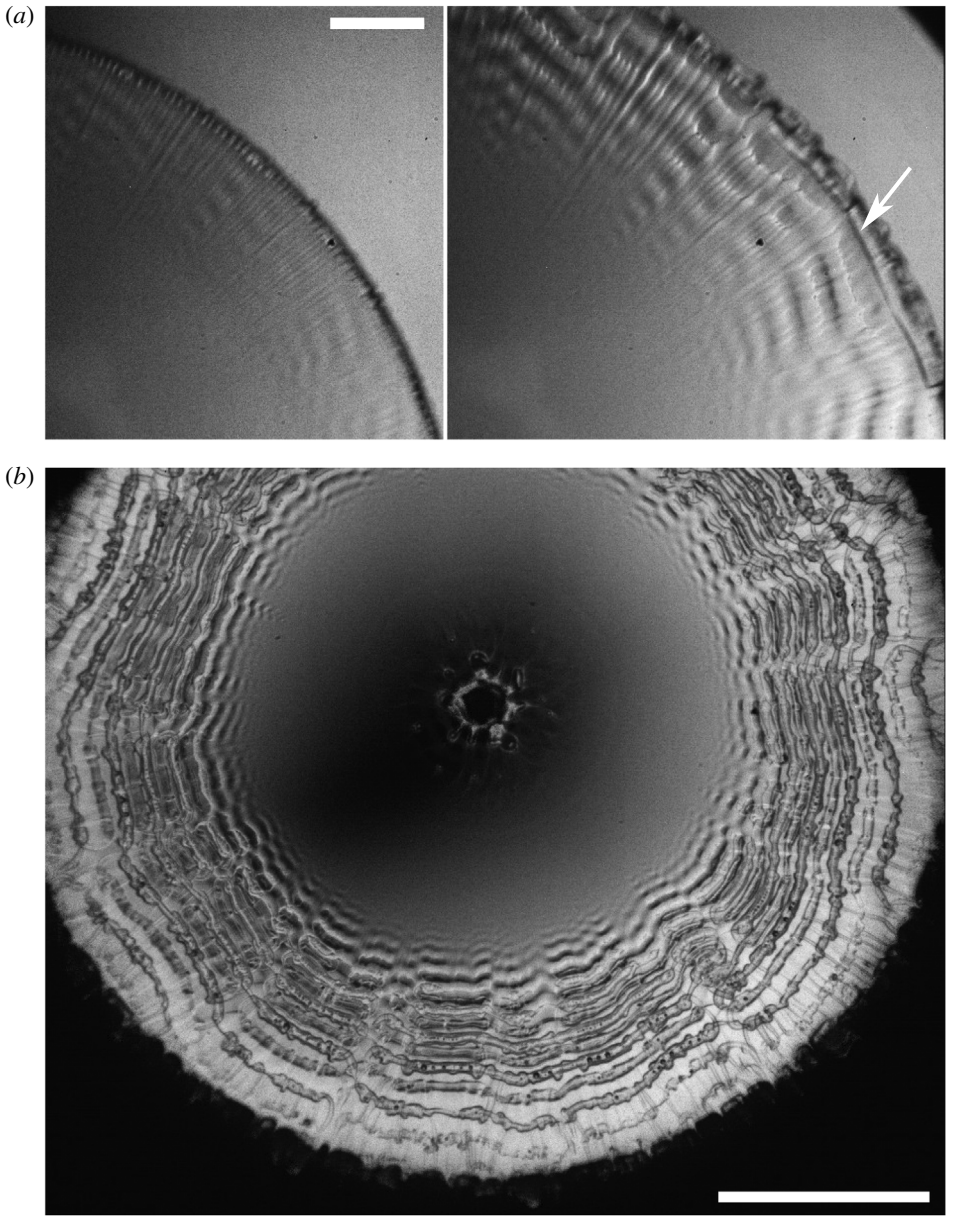


FIGURE 5. Coexistence of radial and azimuthal lines, for $U = 2.87$ m s^{-1}, $\alpha = 0.787$, giving $Re_\alpha = 16\,700$ and $We_\alpha = 737$. (*a*) Close-up of the shape of the edge. Frames are shown 10 and 15 μs after first contact. The arrow points at an air cylinder being entrained. The scale bar is 100 μm long. (*b*) Rows of numerous vortices shed from around the periphery, revealing up to 15 separate vortices, shown at $t = 43$ μs, for the same impact conditions. Scale bar is 500 μm. Initial velocity of the outer edge $\simeq 56$ m s^{-1}. For reference the drop diameter is ∼2 times the width of this image. See also supplementary movies 3 and 4.

https://doi.org/10.1017/jfm.2018.383 Published online by Cambridge University Press

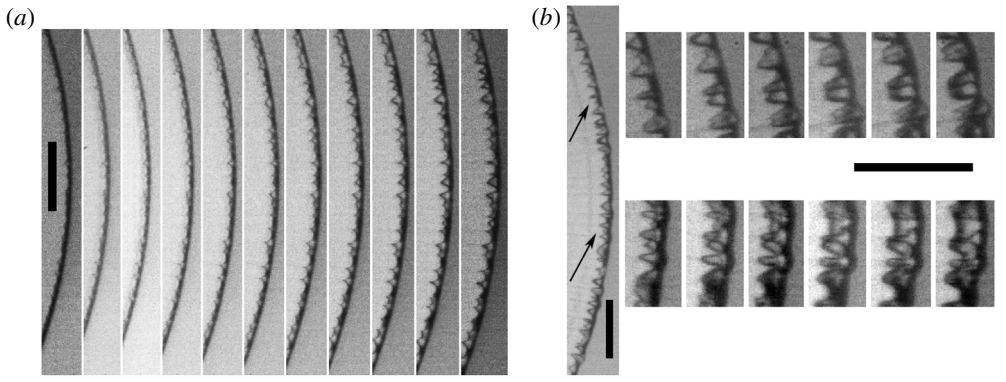


FIGURE 6. (*a*) Growth of the teeth for $U = 2.38$ m s^{-1}, d$t = 0.5$ μs. (*b*) Evidence of air sheets on both sides of the ejecta, marked by the arrows. The relative times of these frames are $t = 0$, 1.0, 2.20, 2.8, 3.6, 4.0 and 4.6 μs. Scale bars are 100 μm long.

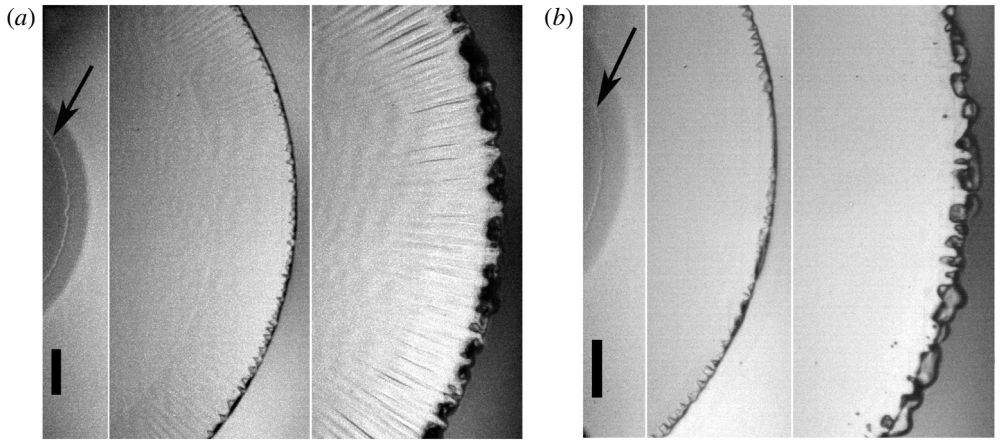


FIGURE 7. Comparison of edge undulations for identical water drops impacting on (*a*) a pool of saturated salt solution ($t \simeq 0.5$, 20, 34 μs) and (*b*) pure water pool ($t \simeq 0.4$, 15, 29 μs). Both for $U = 2.38$ m s^{-1}, $\alpha = 0.828$, giving $Re_\alpha = 13\,000$ and $We_\alpha = 473$. The arrows point at the outer edge of the central air disc. The scale bars are 100 μm long.

The inviscid Wagner theory of Semenov *et al.* (2015) includes impact of different-density fluids. It deals mostly with much larger density ratios, but shows that the ejecta can bend away from the heavier fluid. This would be of interest to study for liquids with larger density differences.

Marangoni effects, due to difference between σ_{drop} and σ_{pool}, should be absent in the sharp corners, as the ejecta separates the two free surfaces, as sketched in figure 1(*c*). Numerical simulations do indeed show the upper part of the ejecta comes from the drop and its lower part from the pool, see for example Josserand & Zaleski (2003), Thoraval *et al.* (2012, 2013). Same is true for inviscid theory (Howison *et al.* 2005; Semenov *et al.* 2015). Semenov *et al.* (2015) show that when the drop becomes much denser than the pool, the triple line shifts along the upper side of the ejecta, thus approaching the neck region. However, even at $\rho_{drop}/\rho_{pool} = 20$ it has not reached the

https://doi.org/10.1017/jfm.2018.383 Published online by Cambridge University Press

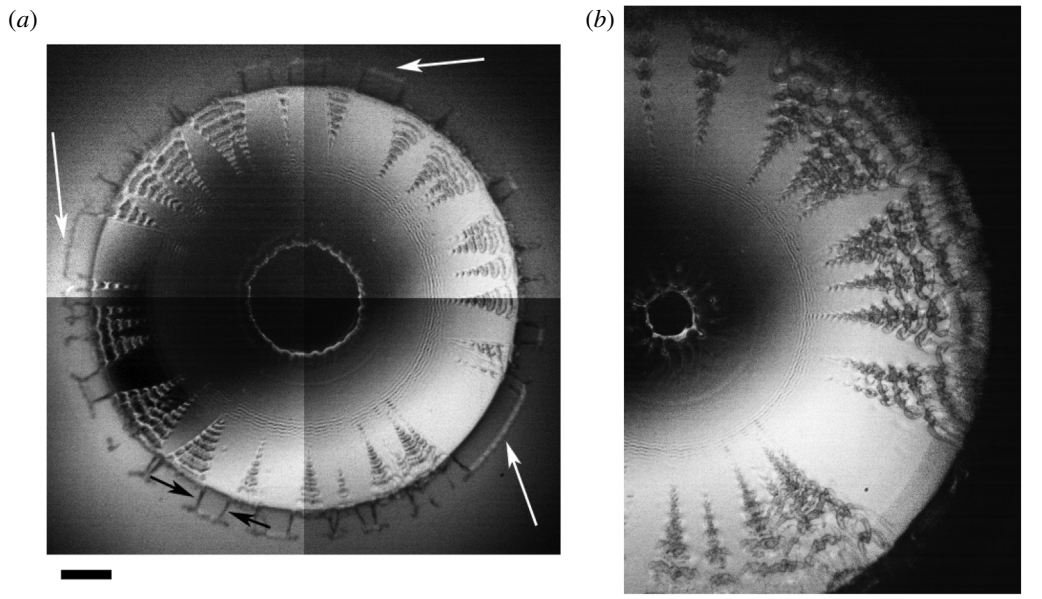


FIGURE 8. Uneven vortex-induced ejecta breakup around the periphery of the neck. (*a*) $t = 17$ μs and (*b*) $t = 47$ μs. Both for $U = 3.09$ m s^{-1}, $\alpha = 0.79$, $Re_\alpha = 17\,900$ and $We_\alpha = 848$. The white arrows point out intact sections of ejecta sheet. Black arrows show the sideways contraction of the edge of the ejecta. The scale bar is 200 μm long. The contrast has been enhanced separately in the four sectors of part (*a*). See supplementary movie 5.

neck. It would therefore require a very strong $\Delta\sigma$ driving motions faster than the ejecta velocity, to bring the affected interface region to the neck. Furthermore, only one neck would be affected, while we see instability in both sharp corners at the base of the ejecta. Also, figure 7(*b*) above shows that the instability shapes persist when the drop and pool are of the same liquid.

4.2. *Importance and nature of the azimuthal instabilities*

What is the significance of these undulations and vortices on the splashing dynamics? Thoraval *et al.* (2012) proposed that the onset of random splashing coincides with the axisymmetric shedding of alternating vortices at the base of the ejecta. Figure 8(*a*) shows a clear demonstration of this importance of the vortex shedding on the breakup of the ejecta, which is here imprinted on a single impact. It shows an anomalous realization where the shedding is non-uniform along the periphery, triggered by localized disturbances in the pool liquid. The ejecta sheet is only visible in the sectors without the vortex shedding, see white arrows. The edges of the intact sections of the sheet contract azimuthally, as indicated by the black arrows. The edge contracts sideways at ∼30 m s^{-1}, indicating a very thin sub-micron liquid sheet. Figure 8(*b*) shows how these localized disturbances can trigger chains of vortices, which look like Christmas trees. These grow rapidly in the azimuthal direction and merge. In these realizations, taken early morning, the salt solution may have precipitated some isolated crystals. These forms were not easily reproducible, but persisted for a number of adjacent realizations. Methods of introducing isolated disturbances in a controlled fashion warrant further study. The presence of the radial vortices can clearly influence the primary vortex shedding, especially in the lower range of Re_α. See also supplementary movie 6.

https://doi.org/10.1017/jfm.2018.383 Published online by Cambridge University Press

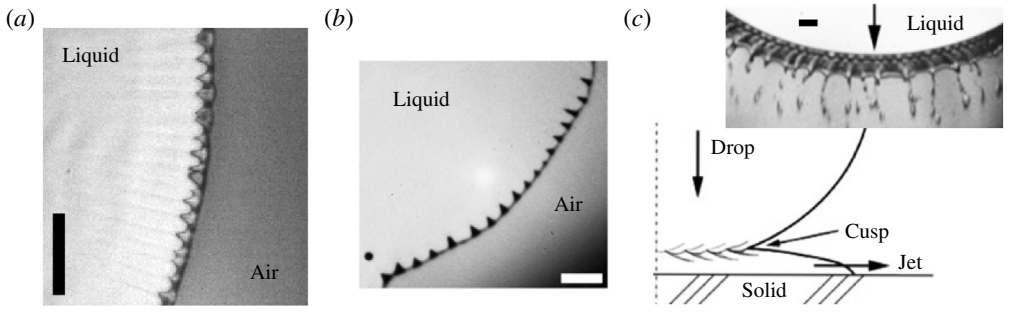


FIGURE 9. Triangular edge shapes for retracting air sheets in three different configurations. (*a*) Close up of the front for the conditions in figure 4(*b*). (*b*) The edge of a rupture in a thin air layer during Mesler entrapment, taken from figure 4(*c*) in Thoroddsen *et al.* (2012*b*). (*c*) Undulations in the sharp corner between drop and lamella, when a drop impacts on a solid surface. Modified from figure 1 in Thoroddsen *et al.* (2012*a*). The scale bars are 100 μm long.

Spanwise instabilities of the edges of liquid sheets or thin air films are intrinsic (Reyssat & Quéré 2006; Villermaux 2007; Craster & Matar 2009; Zhang *et al.* 2010; Agbaglah *et al.* 2013). Regular triangular teeth have also been observed before (Thoroddsen *et al.* 2012*a*,*b*; Gordillo *et al.* 2014). These instabilities are most frequently driven by capillarity, while we believe viscosity plays a role in the triangular form. Figure 9 shows three separate sharp air-corner configurations, all of which develop azimuthal patterns. Panel (*a*) shows the present drop on pool impact, while (*b*) is from the rupture of a thin air film. Finally, part (*c*) shows fine azimuthal structures observed during a drop impact on a solid surface. We therefore conclude that the focus should not be on capillary instabilities at the tip of the ejecta (Weiss & Yarin 1999), but rather in the sharp corners which develop on its two sides (see figure 1*c*). On the other hand, perhaps Rayleigh instability of the tip helps destabilize the corners. We can see whether this is plausible by inferring the ejecta thickness δ from the initial azimuthal wavelength of the triangular pattern, using $\langle N\rangle$ and R_s from figure 3(*b*). Based on this, $\delta \simeq 0.2218 \times 2\pi R_s/\langle N\rangle$, which for our impacts reduces from 34 to 8 μm as We_α increases over our range. These thicknesses are quantitatively similar to those measured in Thoroddsen (2002), but the ejecta thickness cannot be measured in the current experiments.

Vorticity is produced by flow along a curved free surface, see § 5.14 in Batchelor (1967). Once these azimuthal undulations have formed, the flow past the triangular three-dimensional free surfaces will produce both radial and azimuthal components of vorticity (Peck & Sigurdson 1998), the former of which will promote the formation of the observed radial lines. We propose by the symmetry that the surfaces leading to the tip of each triangular shape will promote opposite-sign vortices trailing radially into the neck liquid.

The very similar triangular shapes appearing for the pressure-driven impact ejecta and for the rupture of an air film from rest, may be coincidental, or suggest that the rapid deceleration of the ejecta base is not important. The liquid flow fields around the edge are qualitatively different in these two cases. For the rupture edge, one can expect the capillary number $\mu U/\sigma$, to be important for the balance of σ and ν. For the two impact cases (figure 9*a*,*c*) the flow wraps around the edge without a stagnation point. The asymptotic stability of

https://doi.org/10.1017/jfm.2018.383 Published online by Cambridge University Press

such flow was recently studied by Moore *et al.* (2014), including σ and ν. While a capillary instability wavelength above is consistent with the thickness of the emerging ejecta sheet, which is bounded by two sharp corners, the drop-on-solid impact only has one sharp corner, with a bound lamella.

We suggest the inviscid axisymmetric base flow, around one of the sharp corners at the base of the ejecta, moving for example from the drop and entering into the ejecta sheet, will be unstable to azimuthal undulations. An azimuthal undulation will introduce a change in the radial distance from the axis of symmetry, which will change the local sharpness of the corner based on its axial base geometry. Smaller neck radius will produce a locally sharper corner, which in turn leads to larger velocity and enhanced Bernoulli suction pressure, needed to turn the flow through a larger angle. This pulls the free surface in the corner further towards the axis, making it still sharper which is turn reduces the pressure even more, producing a reinforcing feedback. Surface tension will also become stronger as the corner curvature increases, thereby stopping the growth in amplitude and helping form the secondary three-dimensional flow around the triangular shapes.

We should also mention the possibility of a Rayleigh–Taylor instability of a decelerated density interface, where the fastest growing instability mode is $k_{max} = \sqrt{\rho\, a/(3\sigma)}$, where a is the deceleration. The neck radius is rapidly decelerating, as can be calculated by twice differentiating equation (3.1). This does predict wavelengths of the right order of magnitude. As an example, the front in the first image of figure 4(*a*) is decelerating at $\sim 10^6$ m s^{-2}, giving a wavelength of maximum growth of $\lambda_{max} = 2\pi/k_{max} \simeq 68$ μm. For comparison the measured wavelength in the image is $\lambda \simeq 14$ μm. One problem with this argument is when to calculate the deceleration, as the instability does not appear immediately following first contact, when the deceleration is largest. Of more concern is the true role of surface tension in our configuration. The largest surface curvature is not, in the axial, in the direction of the instability, so how azimuthal undulations would affect the capillary pressure is not clear.

4.3. *Summary*

Herein, we have investigated the earliest dynamics following the contact between a drop impacting a liquid surface. Our focus is on the outer contact where the ejecta sheet emerges. We have shown that for $Re_\alpha > 7000$ the neck region develops fine azimuthal undulations, thereby loosing axisymmetry. Similar undulations were first reported by Thoraval *et al.* (2013), but here we reveal the onset and details of their structure. Using salt solutions in a pool, we are able to observe clear radial striations emanating from these tooth-like patterns in the neck region. These undulations are consistent with capillary instability in the neck. The undulations can occur on both sides of the ejecta and promote the formation of minute triangular air sheets.

The azimuthal instability occurs earlier and independently of the axisymmetric vortex shedding discovered by Thoraval *et al.* (2012). This is clear from the appearance of the radial streaks in figure 4(*a*) at very small neck radii, before any axisymmetric shedding is observed. The presence of this earlier instability explains why the azimuthal vortices are never perfectly axisymmetric around the entire periphery.

Many possible extensions arise from this work. Fully three-dimensional numerical simulations will be needed to capture the vortex structure in the neck region, as well as to see the interactions between the two sides of the base of the ejecta. To pin down the relative importance of viscosity and surface tension in this instability, experiments must be conducted with a range of different liquids and for larger impact velocities.

https://doi.org/10.1017/jfm.2018.383 Published online by Cambridge University Press

Acknowledgements

The work reported herein was funded by King Abdullah University of Science and Technology (KAUST) under grant URF/1/2621-01-01. E.Q.L. acknowledges the Thousand Young Talents Program of China, the National Natural Science Foundation of China (grants nos 11772327, 11642019 and 11621202) and Fundamental Research Funds for the Central Universities (grant no. WK2090050041). M.-J.T. acknowledges the financial support from the National Natural Science Foundation of China (grant nos 11542016 and 11702210) and the 111 project (B18040). M.-J.T. is also supported by the Cyrus Tang Foundation through the Tang Scholar program, and by the Thousand Young Talents Program of China. We thank W. Chan and K. Taylor at Specialized Imaging for their assistance.

Supplementary movies

Supplementary movies are available at https://doi.org/10.1017/jfm.2018.383.

REFERENCES

AGBAGLAH, G., JOSSERAND, C. & ZALESKI, S. 2013 Longitudinal instability of a liquid rim. *Phys. Fluids* **25**, 022103.

BATCHELOR, G. K. 1967 *An Introduction to Fluid Dynamics*. Cambridge University Press.

BOUWHUIS, W., VAN DER VEEN, R. C. A., TRAN, T., KEIJ, D. L., WINKELS, K. G., PETERS, I. R., VAN DER MEER, D., SUN, C., SNOEIJER, J. H. & LOHSE, D. 2012 Maximal air bubble entrainment at liquid-drop impact. *Phys. Rev. Lett.* **109**, 264501.

CASTREJON-PITA, A. A., CASTREJON-PITA, J. R. & HUTCHINGS, I. M. 2012 Experimental observation of von Karman vortices during drop impact. *Phys. Rev.* E **86**, 045301(R).

CRASTER, R. V. & MATAR, O. K. 2009 Dynamics and stability of thin liquid films. *Rev. Mod. Phys.* **81**, 1131–1198.

CROOKS, J., MARSH, B., TURCHETTA, R., TAYLOR, K., CHAN, W., LAHAV, A. & FENIGSTEIN, A. 2013 Kirana: a solid-state megapixel uCMOS image sensor for ultrahigh speed imaging. *Proc. SPIE* **8659**, 865903.

DEEGAN, R. D., BRUNET, P. & EGGERS, J. 2008 Complexities of splashing. *Nonlinearity* **21**, C1–C11.

ETOH, T. G. *et al.* 2003 An image sensor which captures 100 consecutive frames at 1000000 frames/s. *IEEE Trans. Electron Devices* **50**, 144–151.

GORDILLO, J. M., LHUISSIER, H. & VILLERMAUX, E. 2014 On the cusps bordering liquid sheets. *J. Fluid Mech.* **754**, R1.

HENDRIX, M. H. W., BOUWHUIS, W., VAN DER MEER, D., LOHSE, D. & SNOEIJER, J. H. 2016 Universal mechanism for air entrainment during liquid impact. *J. Fluid Mech.* **789**, 708–725.

HICKS, P. D., ERMANYUK, E. V., GAVRILOV, N. V. & PURVIS, R. 2012 Air trapping at impact of a rigid sphere onto a liquid. *J. Fluid Mech.* **695**, 310–320.

HICKS, P. D. & PURVIS, R. 2010 Air cushioning and bubble entrapment in three-dimensional droplet impacts. *J. Fluid Mech.* **649**, 135–163.

HOWISON, S. D., OCKENDON, J. R., OLIVER, J. M., PURVIS, R. & SMITH, F. T. 2005 Droplet impact on a thin fluid layer. *J. Fluid Mech.* **542**, 1–23.

JOSSERAND, C. & THORODDSEN, S. T. 2016 Drop impact on a solid surface. *Annu. Rev. Fluid Mech.* **48**, 365–391.

JOSSERAND, C. & ZALESKI, S. 2003 Droplet splashing on a thin liquid film. *Phys. Fluids* **15**, 1650–1657.

KOROBKIN, A. A. 2007 Second-order Wagner theory of wave impact. *J. Engng Maths* **58**, 121–139.

KOROBKIN, A. A., ELLIS, A. S. & SMITH, F. T. 2008 Trapping of air in impact between a body and shallow water. *J. Fluid Mech.* **611**, 365–394.

KOROBKIN, A. A. & SCOLAN, Y. M. 2006 Three-dimensional theory of water impact. Part 2. Linearized Wagner problem. *J. Fluid Mech.* **549**, 343–373.

https://doi.org/10.1017/jfm.2018.383 Published online by Cambridge University Press

LI, E. Q. & THORODDSEN, S. T. 2015 Time-resolved imaging of a compressible air disc under a drop impacting on a solid surface. *J. Fluid Mech.* **780**, 636–648.

MARSTON, J. O., VAKARELSKI, I. U. & THORODDSEN, S. T. 2011 Bubble entrapment during sphere impact onto quiescent liquid surfaces. *J. Fluid Mech.* **680**, 660–670.

MOORE, M. R., OCKENDON, H., OCKENDON, J. R. & OLIVER, J. M. 2014 Capillary and viscous perturbations to Helmholtz flows. *J. Fluid Mech.* **742**, R1.

OLIVER, J. M. 2002 Water entry and related problems. PhD thesis, Oxford University.

PECK, B. & SIGURDSON, L. 1998 On the kinematics at a free surface. *IMA J. Appl. Maths* **61**, 1–13.

PHILIPPI, J., LAGRÉE, P.-Y. & ANTKOWIAK, A. 2016 Drop impact on a solid surface: short-time self-similarity. *J. Fluid Mech.* **795**, 96–135.

PROSPERETTI, A., CRUM, L. A. & PUMPHREY, H. C. 1989 The underwater noise of rain. *J. Geophys. Res.* **94** (C3), 3255–3259.

REYSSAT, E. & QUÉRÉ, D. 2006 Bursting of a fluid film in a viscous environment. *Europhys. Lett.* **76** (2), 236–242.

RIBOUX, G. & GORDILLO, J. M. 2014 Experiments of drops impacting a smooth solid surface: a model of the critical impact speed for drop splashing. *Phys. Rev. Lett.* **113**, 024507.

RIOBOO, R., MARENGO, M. & TROPEA, C. 2002 Time evolution of liquid drop impact onto solid, dry surfaces. *Exp. Fluids* **33**, 112–124.

SCOLAN, Y. M. & KOROBKIN, A. A. 2001 Three-dimensional theory of water impact. Part 1. Inverse Wagner problem. *J. Fluid Mech.* **440**, 293–326.

SEMENOV, Y. A., WU, G. X. & KOROBKIN, A. A. 2015 Impact of liquids with different densities. *J. Fluid Mech.* **766**, 5–27.

THORAVAL, M.-J., TAKEHARA, K., ETOH, T. G., POPINET, S., RAY, P., JOSSERAND, C., ZALESKI, S. & THORODDSEN, S. T. 2012 Von Kármán vortex street within an impacting drop. *Phys. Rev. Lett.* **108**, 264506.

THORAVAL, M.-J., TAKEHARA, K., ETOH, T. G. & THORODDSEN, S. T. 2013 Drop impact entrapment of bubble rings. *J. Fluid Mech.* **724**, 234–258.

THORODDSEN, S. T. 2002 The ejecta sheet generated by the impact of a drop. *J. Fluid Mech.* **451**, 373–381.

THORODDSEN, S. T., ETOH, T. G. & TAKEHARA, K. 2008 High-speed imaging of drops and bubble. *Annu. Rev. Fluid Mech.* **40**, 257–285.

THORODDSEN, S. T., TAKEHARA, K. & ETOH, T. G. 2012*a* Micro-splashing by drop impacts. *J. Fluid Mech.* **706**, 560–570.

THORODDSEN, S. T., ETOH, T. G. & TAKEHARA, K. 2003 Air entrapment under an impacting drop. *J. Fluid Mech.* **478**, 125–134.

THORODDSEN, S. T., THORAVAL, M.-J., TAKEHARA, K. & ETOH, T. G. 2012*b* Micro-bubble morphologies following drop impacts onto a pool surface. *J. Fluid Mech.* **708**, 469–479.

TRAN, T., DE MALEPRADE, H., SUN, C. & LOHSE, D. 2013 Air entrainment during impact of droplets on liquid surfaces. *J. Fluid Mech.* **726**, R3.

VILLERMAUX, E. 2007 Fragmentation. *Annu. Rev. Fluid Mech.* **39**, 419–446.

WAGNER, H. 1932 Uber Stoss- und Gleitvorgange an der Oberflache von Flussigkeiten. *Z. Angew. Math. Mech.* **12**, 193–215.

WEISS, D. A. & YARIN, A. L. 1999 Single drop impact onto liquid films: neck distortion, jetting, tiny bubble entrainment, and crown formation. *J. Fluid Mech.* **385**, 229–254.

WORTHINGTON, A. M. 1908 *A Study of Splashes*. Longmans, Green and Co.

ZHANG, L. V., BRUNET, P., EGGERS, J. & DEEGAN, R. D. 2010 Wavelength selection in the crown splash. *Phys. Fluids* **22**, 122105.

ZHANG, L. V., TOOLE, J., FEZZAA, K. & DEEGAN, R. D. 2012 Evolution of the ejecta sheet from the impact of a drop with a deep pool. *J. Fluid Mech.* **690**, 5–15.

https://doi.org/10.1017/jfm.2018.383 Published online by Cambridge University Press